ACS Photonics

pubs.acs.org/journal/apchd5

Article

Active Perovskite Hyperbolic Metasurface

Zhitong Li, Joseph S. T. Smalley, Ross Haroldson, Dayang Lin, Roberta Hawkins, Abouzar Gharajeh, Jiyoung Moon, Junpeng Hou, Chuanwei Zhang, Walter Hu, Anvar Zakhidov, and Qing Gu*

Cite This: *ACS Photonics* 2020, 7, 1754−1761

Read Online

ACCESS | Metrics & More | Article Recommendations | Supporting Information

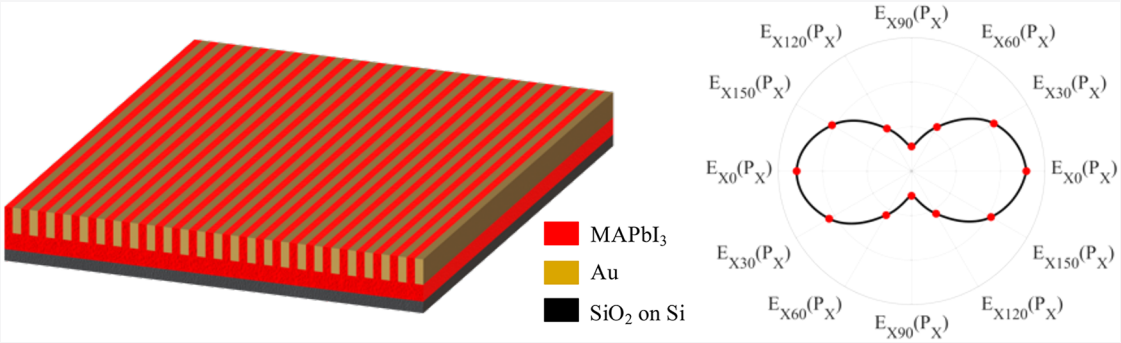

ABSTRACT: A special class of anisotropic media, hyperbolic metamaterials and metasurfaces (HMMs), has attracted much attention in recent years due to its unique ability to manipulate and engineer electromagnetic waves on the subwavelength scale. Because all HMM designs require metal−dielectric composites, the unavoidable metal loss at optical frequencies inspired the development of active HMMs, wherein a gain material is incorporated to compensate for the metal loss. Here, we experimentally demonstrate a luminescent active HMM on silicon that operates at near 750 nm, in which the dielectric constituent is composed entirely of a solution-processed metal-halide perovskite gain. We show the extreme anisotropy of the HMM with microphotoluminescence measurements through the observation of high degrees of linear polarization that are greater than 0.8 in both the emission and absorption. Thanks to the facile fabrication, wide-wavelength tunability, and silicon compatibility for our active HMM, this work paves the way toward HMM's integration into on-chip components and, eventually, photonic integrated circuits.

KEYWORDS: *perovskite, hyperbolic metamaterials, polarization anisotropy, luminescent metasurface, loss compensation*

Metamaterials, artificial materials that have characteristic dimensions much less than their operating wavelengths, have provided a fascinating platform to engineer and manipulate permittivities and, thus, optical properties of materials in dimensions below the diffraction limit.[1] A unique class of metamaterial is hyperbolic metamaterials (HMMs), also known as indefinite media, in which the principle components of the effective permittivity tensor have opposite signs. Namely, they exhibit metal and dielectric properties at the same time.[2−7] As a consequence, the isofrequency surface becomes unbounded, i.e., hyperbolic, in the momentum space (k-space), and the optical density of states (DOS) becomes theoretically infinite.[8]

Since their inception in 2003,[9] HMMs have been investigated for many applications, including super-resolution imaging,[10−13] spontaneous emission enhancement,[14,15] and topological photonics.[16,17] Although various HMMs have been experimentally demonstrated (see Supporting Information (SI) part I for a description of HMM classifications), because of the metal−dielectric composite nature of optical HMM designs, many of HMM's unique features cannot be accessed because of the large metal loss at optical frequencies. It is therefore critical to compensate the metal loss in optical HMMs in order to utilize their full functionalities and eventually insert them into optical devices. One approach to compensate loss is to incorporate gain materials, which led to the development of the second-generation HMM, also termed an active HMM.[2,18] In visible wavelengths, organic dye[15,19] and 2D material[20] gain have been used due to their low cost and facile fabrication.[2] However, because organic dyes can only be dispersed into dielectrics and 2D materials can only be placed onto the HMM surface, the dielectric component is only partially composed of gain, and the resulting loss compensation is not optimal. Recently, a full replacement of the passive dielectric by gain

Received: March 10, 2020
Published: June 9, 2020

https://dx.doi.org/10.1021/acsphotonics.0c00391
ACS Photonics 2020, 7, 1754−1761

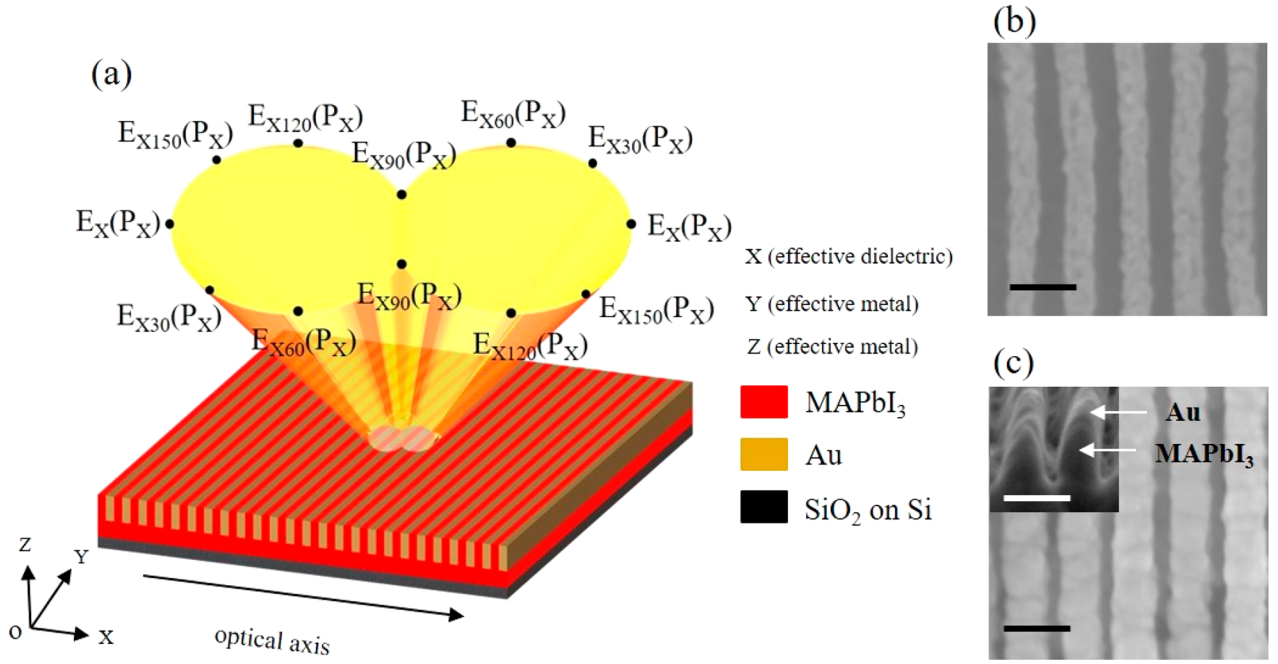

Figure 1. Type II active $MAPbI_3$/Au HMM. (a) Schematic of the deep-subwavelength alternating layers of $MAPbI_3$ (red) and Au (gold) on a Si platform (black). The beam emerging from the HMM surface represents highly anisotropic emission, where the emission is strong in the X direction and weak in the Y direction. (b) Top view SEM image of the $MAPbI_3$ nanograting after NIL. The scale bar is 100 nm. (c) Top view the SEM image of the fabricated active HMM ($MAPbI_3$ nanograting after Au deposition). The scale bar is 100 nm. (Inset) Side view of the SEM image of the active HMM.

was achieved in telecommunication wavelengths in a Ag/InGaAsP multilayer (i.e., type II HMM) by Smalley et al.,[21] in which the active dielectric constituent is an InGaAsP nanograting defined by e-beam lithography followed by dry etching. Despite the success, this approach has not been adapted to shorter wavelengths, possibly due to the difficulty in constructing deep-subwavelength nanogratings of high aspect ratios in epitaxially grown inorganic gain media.

In this work, we demonstrate a luminescent active $MAPbI_3$ perovskite/Au type-II HMM in the wavelength range of 740−780 nm. The choice of $MAPbI_3$ gain allows for the construction of nanogratings of narrow widths and high aspect ratios,[22] and many of perovskite's characteristics (such as low-temperature solution processability,[23] easy bandgap tunability,[24] and large charge-carrier mobility[25]) are all desired features of optical gain. Because a stronger hyperbolic behavior is correspondent with stronger anisotropy, through micro-photoluminescence (micro-PL) measurements, we characterize both the emission and absorption polarization anisotropies to quantify the hyperbolicity in our active HMM.[21] Numerically, we model the fabricated dielectric-metal composite and draw comparisons to the effective medium approximation, isofrequency surface analysis, and negative refraction simulations to verify our HMM's hyperbolic behavior. It is noteworthy that, because the optical axis of our active HMM lies tangential to the plane of the substrate, we regard the HMM as an active hyperbolic metasurface.[19,25]

Our work marks the first active HMM operating below 1 μm, wherein the dielectric constituent is solely composed of a semiconductor gain material. Its realization on the silicon platform further facilitates HMM's integration with optoelectronic components on-chip. In addition, our fabrication method can be readily adapted to visible wavelengths by replacing $MAPbI_3$ with other perovskite compositions. Because perovskites simultaneously function as emitters and constituent dielectrics, our luminescent active HMM can be utilized as a light source with a tailorable emission polarization. This work opens a path toward HMM's insertion into on-chip devices,[26] such as a high-speed light source, an electro-optical modulator, and a perfect light absorber, and HMM's incorporation into applications such as super-resolution imaging and lithography and topological photonics.

RESULTS

The deep-subwavelength $MAPbI_3$ and Au type-II HMM are shown in Figure 1(a). We choose $MAPbI_3$ among all perovskite compositions due to its longest emission wavelength and, in turn, its ease of fabrication in constructing the dielectric nanograting; we choose Au for its low loss at optical frequencies and minimal chemical reaction with perovskites. As shown in Figure 1, the optical axis is defined along the Bloch vector,[27] and X, Y, and Z directions are defined such that the X direction is along the optical axis, while Y and Z directions are orthogonal to the optical axis. To simplify expressions in the proceeding sections, we use notation E_A (P_B) to represent the polarization state of emitted (pump) light. For emission polarization E_A, the subscript A denotes the polarization state, and it can be X (polarization state along the X direction), Y (polarization state along the Y direction), or T (total emission). This subscript is then followed by a number representing the polarization angle with respect to the polarization state direction. Similarly, for pump polarization P_B, the subscript letter B denotes the polarization state, and it can be either X (polarization state along the X direction) or Y (polarization state along the Y direction). For example, $E_{X30}(P_Y)$ denotes 30 degree-polarized emission under Y-polarized pumping, and $E_T(P_X)$ denotes total emission under

https://dx.doi.org/10.1021/acsphotonics.0c00391
ACS Photonics 2020, 7, 1754−1761

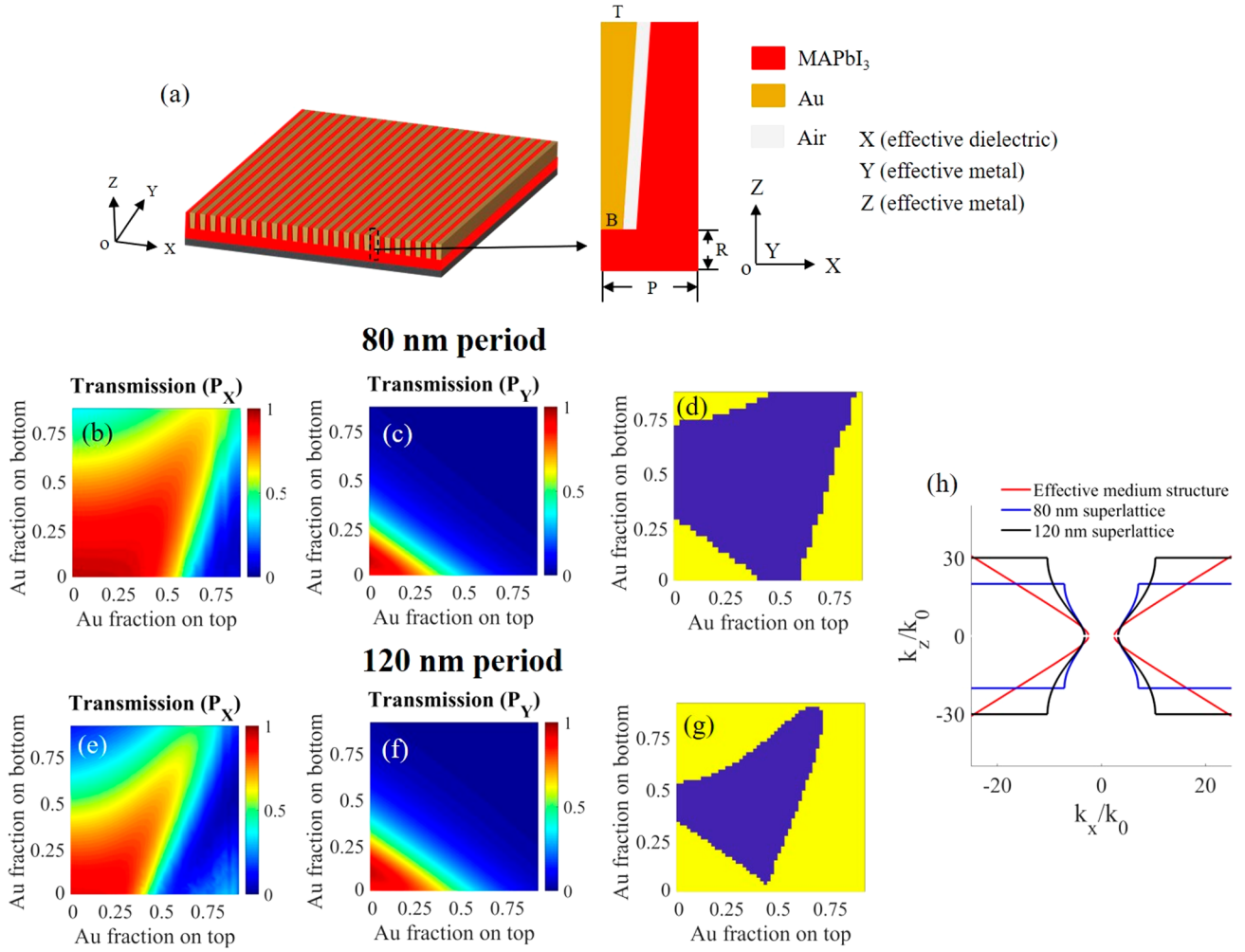

Figure 2. Simulated polarization anisotropy in the active HMM at 765 nm. (a) Side view schematic of one unit-cell. *T* and *B* represent the top and bottom Au widths in one unit-cell, respectively. *R* denotes the residue thickness after NIL. The top and bottom Au fractions are defined by *T*/*P* and *B*/*P*, respectively. The period in (b–d) is 80 nm. (b) Transmission as a function of top and bottom Au fractions with P_X. (c) Transmission as a function of top and bottom Au fractions with P_Y. (d) Identification of the anisotropic region (dark blue). The anisotropic region is defined when transmission is >0.5 with P_X and is <0.5 with P_Y. (e–g) Same as (b–d) but for a 120 nm period. (h) Real part of the isofrequency surface. Blue: transfer matrix theory calculation for a 80 nm period superlattice. Black: transfer matrix theory calculation for a 120 nm period superlattice. Red: effective medium theory calculation.

X-polarized pumping. Lastly, note that E_{Y30} is equivalent to E_{X120} because X and Y directions are orthogonal to each other.

The fabrication of the active HMM consists of three steps, beginning with (i) the construction of a deep-subwavelength nanograting Si stamp using e-beam lithography and inductively coupled plasma (ICP) etching. The resultant stamp is 1.5 cm by 1.5 cm in size, which contains 24 nanograting patterns that are 50 μm by 50 μm in size, 80–120 nm in period with a half duty cycle, and 100 nm in height. (ii) Thermal nanoimprint lithography (NIL) of the perovskite using the Si stamp is used to form a perovskite nanograting, whose geometry is the reverse replica of the stamp. Note that a ∼150 nm thick perovskite residue layer is present after NIL; however, this layer thickness can be changed by adjusting the perovskite thin film thickness. (iii) Thin film evaporation of ∼50 nm Au to partially fill the air trenches is used to form the metal–dielectric multilayer. Figure 1(b) shows the top view scanning electron micrograph (SEM) image of the sample after step (ii), having a perovskite nanograting with a 80 nm period, a half duty cycle, and a 100 nm height. Figure 1(c) shows the top- and side-view SEM images of the resulting superlattice after Au evaporation. Because the fabricated superlattice's period (80–120 nm) is 5–10% of the $MAPbI_3$ photoluminescence (PL) wavelength (700 nm −830 nm), the effective medium approximation can be used. Under the effective medium theory, the principle components of the effective permittivity tensor satisfy real(ε_{XX}) > 0, real(ε_{YY}) < 0, and real(ε_{ZZ}) < 0, fulfilling the requirement for the HMM (see SI part II for calculations). Namely, the superlattice behaves as a dielectric in the X direction and as a metal in the Y and Z directions. Its hyperbolic dispersion can also be verified by negative refraction simulations (SI part III).

Although etched HMM designs usually assume straight nanograting sidewalls,[28] angled sidewalls are inevitable in fabricated structures (Figure 1(c)). To understand the impact of such fabrication imperfections, we examine the expected anisotropy in realistic structures through transmission and reflection simulations. Figure 2 shows light transmission at 765 nm (peak of the $MAPbI_3$ PL spectrum) through HMMs with angled sidewalls and a 10 nm air gap in each unit-cell as functions of the Au fraction at the top and bottom of the superlattice (the Au fraction is defined as the Au width divided

https://dx.doi.org/10.1021/acsphotonics.0c00391
ACS Photonics 2020, 7, 1754–1761

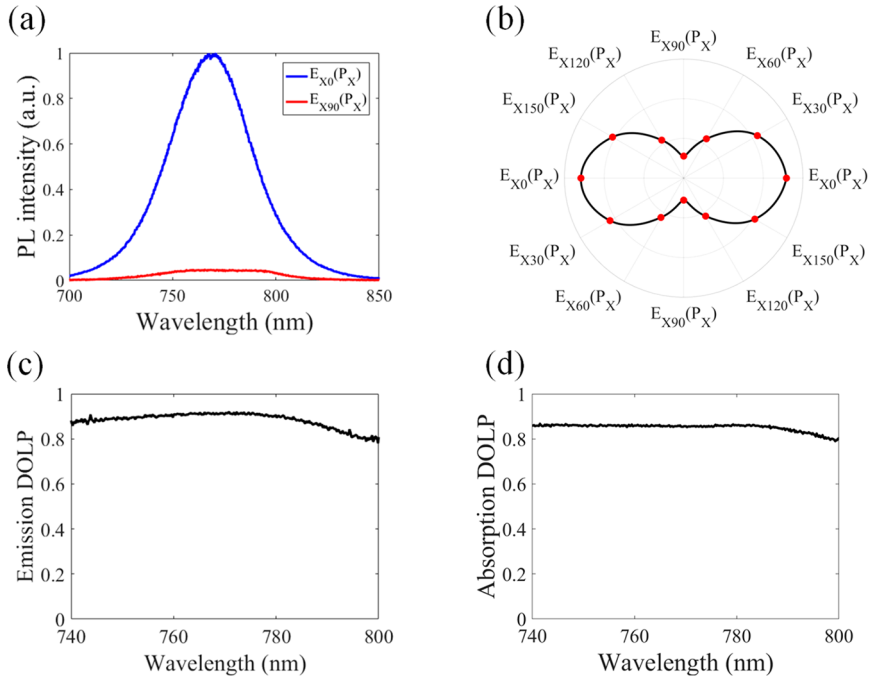

Figure 3. Measured polarization anisotropy of the active HMM. (a) PL spectra with $E_{X0}(P_X)$ (blue) and $E_{X90}(P_X)$ (red). Note that $E_{Xa}(P_X) = E_{X(180-a)}(P_X)$. (b) Angle dependent total emission integrated from 750 to 800 nm. (c) Spectrum of the emission DOLP. (d) Spectrum of the absorption DOLP.

by the lattice period). As the X-polarized incident light (i.e., incident light polarized in the effective dielectric direction) propagates from top to bottom along the Z direction, a high transmission is expected when the Au and $MAPbI_3$ ratio falls within the HMM range. On the other hand, in this range, a low transmission is expected with Y-polarized incident light (in the effective metal direction). Figure 2(b) and (c) show the transmission as functions of the Au fraction on the top and bottom for a superlattice with a 80 nm period, while Figure 2(e) and (f) show the case with a 120 nm period. With the anisotropic region defined as $P_X > 0.5$ and $P_Y < 0.5$, Figure 2(d) and (g) show that a smaller period corresponds to stronger anisotropy, consistent with results of Figure S7. Therefore, to operate in the anisotropic region, both the top and bottom Au fractions should be close to 0.5. We further carry out isofrequency surface calculations to investigate whether hyperbolic dispersion is achieved in such anisotropic media. The isofrequency surface plots for 80 and 120 nm periods are shown in Figure 2(h). The red line is calculated using the effective medium approximation, in which k_z is unbounded. The blue and black lines are calculated using layered $MAPbI_3$/Au through the transfer matrix theory, in which the largest allowable $k_z = \lambda/P \times 2\pi$ is defined by the Bloch theory. In agreement with transmission simulation results, the largest allowable k_z in the case of the 80 nm period (Figure 2(h) blue) is larger than that of the 120 nm period (Figure 2(h) black), i.e., the superlattice with the 80 nm period has a larger hyperbolic region. While the analysis thus far ignores material loss or optical gain, we show that the transmission characteristics remain when material loss is included (Figure S3), and the isofrequency surface features remain when optical gain is present (Figure S11).

To verify our HMM's hyperbolicity, we measure the polarization anisotropy, as the stronger polarization anisotropy is associated with more a prominent hyperbolic behavior. Taking advantage of the luminescent feature of our active HMM, we conduct emission and absorption polarization anisotropy measurements using a micro-PL system (see Methods for details). With an X-polarized 355 nm pump light incident on the HMM, we collect the PL from the HMM after its emission passes through a polarizer. As shown in Figure 3(a) and (b), the highest and lowest emission levels occur at $E_{X0}(P_X)$ and $E_{X90}(P_X)$, respectively. The highest emission level $E_{X0}(P_X)$ has a similar intensity to that from $MAPbI_3$ thin film as well as $MAPbI_3$ nanograting control samples (see SI part IV), indicating a dielectric behavior along the X direction. On the other hand, the lowest emission level $E_{X90}(P_X)$ has a similar intensity to that from an Au-covered $MAPbI_3$ thin film (i.e., outside of the patterned area, as shown in Figure S8(a)), indicating the metal behavior along the Y direction. These results are consistent with the effective medium calculation in Figure S2. Figure 3(b) depicts the evolution of the integrated emission intensity as a function of the emission polarization angle: the intensity gradually drops from the maximum to the minimum from $E_{X0}(P_X)$ to $E_{X90}(P_X)$ and then increases back to the maximum when the polarization reaches $E_{X180}(P_X)$. We conduct the same PL measurement on a $MAPbI_3$ thin film (Figure S8(b)) and dielectric $MAPbI_3$ nanograting (Figure S9) control samples. In both cases, only a slight angle-dependent emission is observed, confirming that the large polarization anisotropy is present only in the HMM.

To quantify the strength of the anisotropy, we calculate the degree of linear polarization (DOLP) for the emitted light and for the absorption of the pump light, respectively. Emission DOLP is defined as $((E_X(P_X) - E_Y(P_X))/((E_X(P_X) + E_Y(P_X))$, wherein a unity DOLP means linearly polarized emission (i.e., extreme anisotropy), while a zero DOLP means isotropic emission. As shown in Figure 3(c), our active HMM's emission is highly anisotropic, with a DOLP above 0.85 and between 740 and 800 nm. This value matches well with the simulated

https://dx.doi.org/10.1021/acsphotonics.0c00391
ACS Photonics 2020, 7, 1754−1761

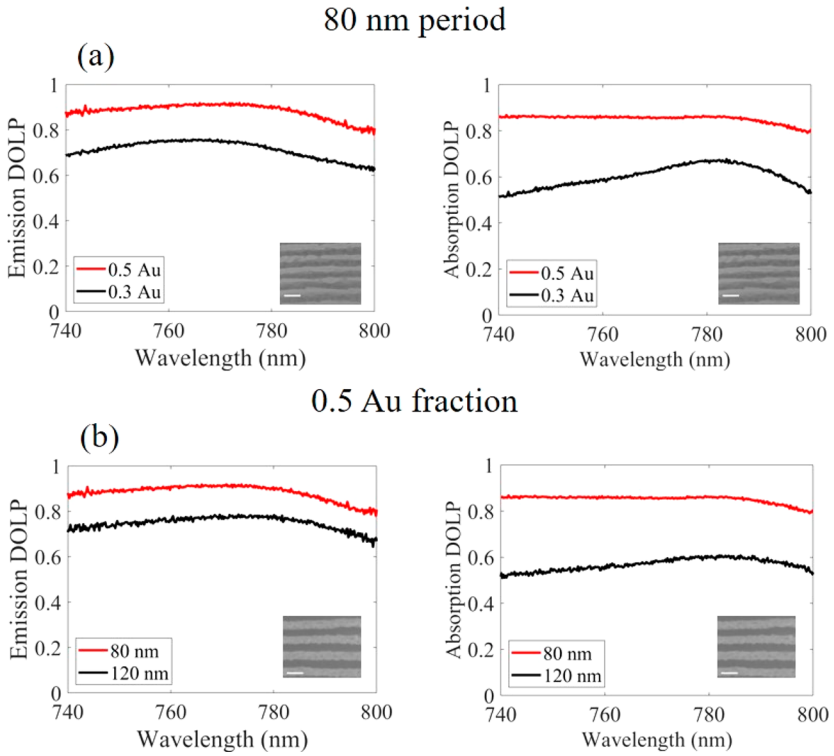

Figure 4. Measured polarization anisotropy in the active HMM. The inset shows the top-view SEM image of the corresponding $MAPbI_3$ nanograting (before Au deposition). (a) Spectrum of the emission and absorption DOLP with an 80 nm period, a 0.5 Au fraction (red, the same as the spectrum in Figure 3(c)), and a 0.3 Au fraction (black). (b) Spectrum of the emission and absorption DOLP with a 0.5 Au fraction, an 80 nm period (red, the same as the spectrum in Figure 3(c)), and a 120 nm period (black).

emission anisotropy (Figure S4). On the other hand, the absorption DOLP is defined as $(E_T(P_X) - E_T(P_Y))/(E_T(P_X) + E_T(P_Y))$. Figure 3(d) shows that our HMM has large absorption anisotropy, with a DOLP above 0.8 and between 740 and 780 nm. Overall, in the fabricated 80 nm period active HMM, a strong polarization anisotropy is present at both the emission (765 nm) and pump (355 nm) wavelengths. It is worth noting that this emission polarization anisotropy primes our active HMM metasurface for light sources with tailorable polarization.

Figure 4 shows the experimental comparison of the anisotropy in active HMMs of different Au fractions and lattice periods. Comparing HMMs of 0.3 and 0.5 Au fractions with the same 80 nm period, Figure 4(a) shows that the lower Au fraction corresponds to a lower DOLP. Similarly, comparing HMMs of different periods with the same 0.5 Au fraction, Figure 4(b) shows that a smaller period corresponds to a higher DOLP. These results are also verified using the effectiveness examination of effective medium theory (SI part V).

CONCLUSION

In summary, we theoretically and experimentally investigated the hyperbolic dispersion in a luminescent active type II HMM composed of a $MAPbI_3$/Au superlattice on silicon, marking the first active HMM below 1 μm. Measurements of the polarization anisotropy, coupled with a systematic theoretical analysis, show the possibility of realizing metamaterials describable by the effective medium theory to achieve extreme anisotropy. The highly anisotropic emission of these luminescent HMMs may lead to new strategies toward designing light sources with a tailorable polarization, and their realization on the silicon platform opens an avenue toward HMM's integration into on-chip components. Thanks to the loss compensation provided by the dielectric constituent fully composed of gain, we are a step closer toward HMM's insertion into applications such as super-resolution imaging and lithography and topological photonics.

METHODS

Deep-Subwavelength Si Stamp Fabrication. The Si-nanograting stamp of an 80−120 nm period, a half duty cycle, and a 100 nm height is fabricated using standard electron beam lithography followed by inductively coupled plasma (ICP) dry etching. A Si substrate is first cleaned via ultrasonication with acetone and isopropyl alcohol (IPA) for 2 min each. Its surface is then treated with SurPass 3000 (DisChem, Inc.) to increase the adhesion to hydrogen silsesquioxane (HSQ) for e-beam resists (Dow Corning XR-1541). A 35 nm thick HSQ layer is then spun-coated onto the substrate in two steps: step 1, using 500 rpm with a 100 rpm/s acceleration for 5 s; step 2, using 3000 rpm with a 3000 rpm/s acceleration for 60 s, followed by 5 min of baking on a hot plate at 90 °C to harden the resist. To resolve the deep-subwavelength grating, 1 line with a 3.5 nC/cm line dose is written in each period using a RAITH-150 e-beam lithography system, at an acceleration voltage of 30 kV and an aperture size of 30 μm. After the patterns are written, the sample is developed in 25% tetramethylammonium hydroxide (TMAH) at 38 °C for 1 min. Next, Cl_2 plasma dry etching is used to define the Si nanograting in an ICP etcher (Plasma Therm, Inc.), with a pressure of 5 mTorr and an ICP power of 500 W, resulting in an etch depth of 100 nm. Finally, HSQ is stripped off in a 7:1 buffered oxide etch (BOE) for 90 s. The resultant stamp is 1.5 cm by 1.5 cm in size, which

https://dx.doi.org/10.1021/acsphotonics.0c00391
ACS Photonics 2020, 7, 1754−1761

contains 24 nanograting patterns that are 50 μm by 50 μm in size.

Perovskite Thin Film Preparation. The $MAPbI_3$ solution is made by dissolving a 1:1 molar ratio of CH_3NH_3I and PbI_2 in a 7:3 volume ratio of γ-butyrolactone (GBL) and dimethylformamide (DMF) solvent mixture in a glovebox. The resulting concentration of the solution is 1.5 M. Next, the solution is heated on a hot plate for 24 h at 60 °C to fully dissolve. Meanwhile, a 1 μm thick SiO_2 film is thermally grown on a Si substrate, followed by cleaning via ultrasonication with acetone and IPA for 1 min each. Before spin-coating, the SiO_2 on the Si substrate is treated with UV−ozone for 15 min to increase the adhesion between the substrate and $MAPbI_3$. The spin-coating of $MAPbI_3$ consists of two steps: step 1, using 1000 rpm with a 1000 rpm/s acceleration for 23 s; step 2, using 4000 rpm with maximum acceleration for 30 s. Then, 12 s into the second spin-coating step, 300 μL of ydrous toluene is dropped onto the film to increase the uniformity. Finally, the sample is annealed at 100 °C on a hot plate for 10 min.

Thermal Nanoimprint Lithography of $MAPbI_3$. The deep-subwavelength Si stamp is first coated with an antiadhesion monolayer of FDTS (1*H*,1*H*,2*H*,2*H*-perfluorodecyltrichlorosilane 96% from Alfa Aesar) to increase the hydrophobicity on the surface for subsequent thermal nanoimprint lithography (NIL). The NIL procedure is performed in an Obducat nanoimprinter. First, the Si stamp is placed on the spin-coated $MAPbI_3$ perovskite film with a 200 nm thickness. To imprint, an aluminum foil is placed onto the stamp with an O-ring to hold up the vacuum. After ensuring that the O-ring is holding the stamp in place, the O-ring is removed, and a poly foil is placed on top of the aluminum foil to increase conformity during NIL. NIL consists of three steps: step 1, the temperature is gradually increased from 35 to 100 °C and the pressure from 0 to 70 bar, with the entire process taking 6 min; step 2, the temperature and pressure are kept at 100 °C for 20 min; step 3, the temperature is gradually dropped from 100 to 35 °C in 14 min. The pressure is kept at 70 bar for the entire 14 min duration and is then suddenly released to 0 bar. Finally, the Si stamp is carefully demolded with a blade along the direction of the nanograting. The resulting $MAPbI_3$ nanograting depth is ∼100 nm with a perovskite residue thickness of 150 nm.

Thin Film Evaporation of Au. After NIL, a 50 nm thick layer of Au is uniformly deposited into the perovskite nanograting in a planetary deposition system (CHA e-gun evaporator) at a chamber pressure of 6×10^{-7} mTorr and with a deposition rate of 0.2 Å/s.

Theoretical Calculation and COMSOL Simulation. Theoretical calculations are performed using the effective medium theory (details are provided in SI part II). Transmission and reflection simulations are carried out using the frequency domain solver with the commercial finite element method (FEM) software of COMSOL Multiphysics. Negative refraction simulations are conducted in the frequency domain solver in COMSOL.

Polarization Anisotropy Characterization. Polarization anisotropy measurements are conducted at room temperature using a steady-state micro-PL spectroscopy system. The X-polarized 355 nm femtosecond pump light (Uranus 1030-005-0350-PM, Laser-Femto), which is focused to a ∼20 μm spot size, is normally incident on the sample being tested through a dichroic mirror and an ultraviolet microscope objective with a numerical aperture (NA) of 0.13. A telescope is used to reduce the chromatic aberration by matching the focal planes of the pump and emission wavelengths. To image the pump beam on the HMM pattern, a visible CCD camera (Ophir SP90281) is used in a microscopy configuration. A long-pass dichroic mirror with a cutoff wavelength of 425 nm is introduced to reflect the pump light (355 nm) onto the sample and to pass the emission (765 nm) from the sample. The emitted light is collected by a spectrograph (Princeton Instruments IsoPlane SCT-320) coupled to a cooled Si detector (Princeton Instruments PIXIS:400BRX). In the emission polarization anisotropy measurements, a polarizer is placed in the emission path to select specific polarization angles. In the pump polarization anisotropy measurements along the Y direction, the X-polarized output beam of the pump laser is rotated to a Y-polarized beam by a quarter wave plate, followed by a polarizer with its T-axis along the Y direction to pass only the Y-polarized beam in the pump path. A schematic of the micro-PL setup is shown in Figure S12.

■ ASSOCIATED CONTENT

Supporting Information

The Supporting Information is available free of charge at https://pubs.acs.org/doi/10.1021/acsphotonics.0c00391.

In part I, Figure S1 shows the isofrequency surface contour of isotropic dielectric, type I and type II HMMs. In part II, the calculation of our perovskite/Au HMM's effective permittivity is presented in Figure S2. In part III, numerical simulations are presented. Figure S3 shows the comparison of the HMM region as functions of the top and bottom Au fractions for the superlattice of different periods. Figure S4 shows the calculated emission DOLP. Figure S5 shows the simulated figure of merits when a thin layer of Au is present on top of the perovskite, as is the case in the fabricated HMM. Figure S6 shows the principle and final results of negative refraction simulations. Figure S7 shows the identification and comparison of different regions (i.e., effective dielectric, effective metal, or HMM) using negative refraction simulations. In part IV, additional measurement results are presented. Figure S8 shows the emission from a Au-covered $MAPbI_3$ thin film and the emission polarization dependency of a $MAPbI_3$ thin film. Figure S9 shows the emission polarization of $MAPbI_3$ nanograting of different periods. In part V, the effectiveness of the effective medium theory is presented in Figure S10. In part VI, the isofrequency surface plots are illustrated in Figure S11 to analyze the loss compensation by the gain material. Figure S12 shows the schematic of the steady-state micro-PL spectroscopy setup (PDF)

■ AUTHOR INFORMATION

Corresponding Author

Qing Gu − *Department of Electrical and Computer Engineering, The University of Texas at Dallas, Richardson, Texas 75080, United States;* orcid.org/0000-0003-3855-3690; Email: qing.gu@utdallas.edu

Authors

Zhitong Li − *Department of Electrical and Computer Engineering, The University of Texas at Dallas, Richardson, Texas 75080, United States*

https://dx.doi.org/10.1021/acsphotonics.0c00391
ACS Photonics 2020, 7, 1754−1761

Joseph S. T. Smalley − *DigiLens, Inc., Sunnyvale, California 94089, United States*
Ross Haroldson − *Department of Physics, The University of Texas at Dallas, Richardson, Texas 75080, United States*
Dayang Lin − *Department of Electrical and Computer Engineering, The University of Texas at Dallas, Richardson, Texas 75080, United States*
Roberta Hawkins − *Department of Materials Science and Engineering, The University of Texas at Dallas, Richardson, Texas 75080, United States*
Abouzar Gharajeh − *Department of Electrical and Computer Engineering, The University of Texas at Dallas, Richardson, Texas 75080, United States*
Jiyoung Moon − *Department of Materials Science and Engineering, The University of Texas at Dallas, Richardson, Texas 75080, United States*
Junpeng Hou − *Department of Physics, The University of Texas at Dallas, Richardson, Texas 75080, United States*
Chuanwei Zhang − *Department of Physics, The University of Texas at Dallas, Richardson, Texas 75080, United States*
Walter Hu − *Department of Electrical and Computer Engineering, The University of Texas at Dallas, Richardson, Texas 75080, United States*
Anvar Zakhidov − *Department of Physics, The University of Texas at Dallas, Richardson, Texas 75080, United States; Department of Nanophotonics and Metamaterials, ITMO University, St. Petersburg 197101, Russia;* orcid.org/0000-0003-3983-2229

Complete contact information is available at: https://pubs.acs.org/10.1021/acsphotonics.0c00391

Funding

This work is supported by the Welch Foundation (Grants AT-1992-20190330 and AT-1617), the National Science Foundation (NSF) under CAREER Award (ECCS-1941629), the Army Research Office (ARO) (W911NF-19-1-0303), and The University of Texas at Dallas Office of Research through the SPIRe Grant Program. J.H. and C.Z. acknowledge support from the AFOSR (FA9550-16-1-0387), NSF (PHY-1806227), and ARO (W911NF-17-1-0128).

Notes

The authors declare no competing financial interest.

REFERENCES

(1) Lemoult, F.; Kaina, N.; Fink, M.; Lerosey, G. Wave Propagation Control at the Deep Subwavelength Scale in Metamaterials. *Nat. Phys.* **2013**, *9* (1), 55−60.
(2) Smalley, J. S. T.; Vallini, F.; Zhang, X.; Fainman, Y. Dynamically Tunable and Active Hyperbolic Metamaterials. *Adv. Opt. Photonics* **2018**, *10* (2), 354−408.
(3) Ferrari, L.; Wu, C.; Lepage, D.; Zhang, X.; Liu, Z. Hyperbolic Metamaterials and Their Applications. *Prog. Quantum Electron.* **2015**, *40*, 1−40.
(4) Poddubny, A.; Iorsh, I.; Belov, P.; Kivshar, Y. Hyperbolic Metamaterials. *Nat. Photonics* **2013**, *7* (12), 948−957.
(5) Guo, Z.; Jiang, H.; Chen, H. Hyperbolic Metamaterials: From Dispersion Manipulation to Application. *J. Appl. Phys.* **2020**, *127*, 071101.
(6) Bang, S.; So, S.; Rho, J. Realization of Broadband Negative Refraction in Visible Range Using Vertically Stacked Hyperbolic Metamaterials. *Sci. Rep.* **2019**, *9* (1), 1−7.
(7) Huo, P.; Zhang, S.; Liang, Y.; Lu, Y.; Xu, T. Hyperbolic Metamaterials and Metasurfaces: Fundamentals and Applications. *Adv. Opt. Mater.* **2019**, *7*, 1801616.
(8) Jacob, Z.; Kim, J. Y.; Naik, G. V.; Boltasseva, A.; Narimanov, E. E.; Shalaev, V. M. Engineering Photonic Density of States Using Metamaterials. *Appl. Phys. B: Lasers Opt.* **2010**, *100* (1), 215−218.
(9) Smith, D. R.; Schurig, D. Electromagnetic Wave Propagation in Media with Indefinite Permittivity and Permeability Tensors. *Phys. Rev. Lett.* **2003**, *90* (7), 077405.
(10) Jacob, Z.; Alekseyev, L. V.; Narimanov, E. Optical Hyperlens: Far-Field Imaging beyond the Diffraction Limit. *Opt. Express* **2006**, *14* (18), 8247−8256.
(11) Liu, Z.; Lee, H.; Xiong, Y.; Sun, C.; Zhang, X. Far-Field Optical Hyperlens Magnifying Sub-Diffraction-Limited Objects. *Science (Washington, DC, U. S.)* **2007**, *315* (5819), 1686.
(12) Lu, D.; Liu, Z. Hyperlenses and Metalenses for Far-Field Super-Resolution Imaging. *Nat. Commun.* **2012**, *3* (1), 1205.
(13) Ma, Q.; Qian, H.; Montoya, S.; Bao, W.; Ferrari, L.; Hu, H.; Khan, E.; Wang, Y.; Fullerton, E. E.; Narimanov, E. E.; Zhang, X.; Liu, Z. Experimental Demonstration of Hyperbolic Metamaterial Assisted Illumination Nanoscopy. *ACS Nano* **2018**, *12* (11), 11316−11322.
(14) Ferrari, L.; Lu, D.; Lepage, D.; Liu, Z. Enhanced Spontaneous Emission inside Hyperbolic Metamaterials. *Opt. Express* **2014**, *22* (4), 4301−4306.
(15) Lu, D.; Kan, J. J.; Fullerton, E. E.; Liu, Z. Enhancing Spontaneous Emission Rates of Molecules Using Nanopatterned Multilayer Hyperbolic Metamaterials. *Nat. Nanotechnol.* **2014**, *9* (1), 48−53.
(16) Hou, J.; Li, Z.; Luo, X. W.; Gu, Q.; Zhang, C. Topological Bands and Triply Degenerate Points in Non-Hermitian Hyperbolic Metamaterials. *Phys. Rev. Lett.* **2020**, *124* (7), 73603.
(17) Hou, J.; Li, Z.; Gu, Q.; Zhang, C. Non-Hermitian Photonics Based on Charge-Parity Symmetry. **2019**, arXiv: physics/1904.05260. *arXiv.org e-Print archive*. https://arxiv.org/abs/1904.05260.
(18) Lu, L.; Simpson, R. E.; Valiyaveedu, S. K. Active Hyperbolic Metamaterials: Progress, Materials and Design. *J. Opt.* **2018**, *20* (10), 103001.
(19) Chandrasekar, R.; Wang, Z.; Meng, X.; Azzam, S. I.; Shalaginov, M. Y.; Lagutchev, A.; Kim, Y. L.; Wei, A.; Kildishev, A. V.; Boltasseva, A.; Shalaev, V. M. Lasing Action with Gold Nanorod Hyperbolic Metamaterials. *ACS Photonics* **2017**, *4* (3), 674−680.
(20) Galfsky, T.; Sun, Z.; Considine, C. R.; Chou, C.; Ko, W.; Lee, Y.; Narimanov, E. E.; Menon, V. M. Broadband Enhancement of Spontaneous Emission in Two- Dimensional Semiconductors Using Photonic Hypercrystals. *Nano Lett.* **2016**, *16* (8), 4940−4945.
(21) Smalley, J. S. T.; Vallini, F.; Montoya, S. A.; Ferrari, L.; Shahin, S.; Riley, C. T.; Kante, B.; Fullerton, E. E.; Liu, Z.; Fainman, Y. Luminescent Hyperbolic Metasurfaces. *Nat. Commun.* **2017**, *8*, 13793.
(22) Mayer, A.; Buchmüller, M.; Wang, S.; Steinberg, C.; Papenheim, M.; Scheer, H.-C.; Pourdavoud, N.; Haeger, T.; Riedl, T. Thermal Nanoimprint to Improve the Morphology of $MAPbX_3$ (MA = Methylammonium, X = I or Br). *J. Vac. Sci. Technol., B: Nanotechnol. Microelectron.: Mater., Process., Meas., Phenom.* **2017**, *35* (6), 06G803.
(23) You, J.; Hong, Z.; Yang, Y. M.; Chen, Q.; Cai, M.; Song, T.-B.; Chen, C.-C.; Lu, S.; Liu, Y.; Zhou, H.; Yang, Y. Low-Temperature Solution-Processed Perovskite Solar Cells with High Efficiency and Flexibility. *ACS Nano* **2014**, *8* (2), 1674−1680.
(24) Liu, W.; Lin, Q.; Li, H.; Wu, K.; Robel, I.; Pietryga, J. M.; Klimov, V. I. Mn2+-Doped Lead Halide Perovskite Nanocrystals with Dual-Color Emission Controlled by Halide Content. *J. Am. Chem. Soc.* **2016**, *138* (45), 14954−14961.
(25) Wehrenfennig, C.; Eperon, G. E.; Johnston, M. B.; Snaith, H. J.; Herz, L. M. High Charge Carrier Mobilities and Lifetimes in Organolead Trihalide Perovskites. *Adv. Mater.* **2014**, *26* (10), 1584−1589.
(26) Lee, C.-H.; Seo, M.-K. Broadband Two-Dimensional Hyperbolic Metasurface for on-Chip Photonic Device Applications. *Opt. Lett.* **2020**, *45* (9), 2502−2505.
(27) Joannopoulos, J. D.; Johnson, S. G.; Winn, J. N.; Meade, R. D. *Photonic Crystals: Molding the Flow of Light*, 2nd ed.; Princeton University Press, 2008

(28) High, A. A.; Devlin, R. C.; Dibos, A.; Polking, M.; Wild, D. S.; Perczel, J.; De Leon, N. P.; Lukin, M. D.; Park, H. Visible-Frequency Hyperbolic Metasurface. *Nature* **2015**, *522* (7555), 192−196.

https://dx.doi.org/10.1021/acsphotonics.0c00391
ACS Photonics 2020, 7, 1754−1761